Catalytic, Spectroscopic, and Theoretical Studies of Fe_4S_4-Based Coordination Polymers as Heterogenous CPET Mediators for Electrocatalysis

Ningxin Jiang[1], Andrea Darù[1], Špela Kunstelj[1], Jenny G. Vitillo[2], Maia E. Czaikowski[1], Alexander S. Filatov[1], Anna Wuttig[1], Laura Gagliardi[1,3], John S. Anderson[1*]

[1]Department of Chemistry, University of Chicago, Chicago, Illinois 60637, United States.

[2]Department of Science and High Technology and INSTM, Università degli Studi dell'Insubria, Como, 22100, Italy.

[3]Pritzker School of Molecular Engineering, James Franck Institute, University of Chicago, Chicago, Illinois 60637, United States.

*Email: jsanderson@uchicago.edu

ABSTRACT: Iron-sulfur clusters play essential roles in biological systems and thus synthetic $[Fe_4S_4]$ clusters have been an area of active research. Recent studies have demonstrated that soluble $[Fe_4S_4]$ clusters can serve as net H-atom transfer mediators, improving the activity and selectivity of a homogeneous Mn CO_2 reduction catalyst. Here, we demonstrate that incorporating these $[Fe_4S_4]$ clusters into a coordination polymer enables heterogeneous H-atom transfer from an electrode surface to a Mn complex dissolved in solution. A previously reported solution-processable Fe_4S_4-based coordination polymer was successfully deposited on the surfaces of different electrodes. The coated electrodes serve as H-atom transfer mediators to a soluble Mn CO_2 reduction catalyst displaying good product selectivity for formic acid. Furthermore, these electrodes are recyclable with a minimal decrease in activity after multiple catalytic cycles. The heterogenization of the mediator also enables the characterization of solution-phase and electrode surface species separately. Surface enhanced infrared absorption spectroscopy (SEIRAS) reveals spectroscopic signatures for an *in-situ* generated active Mn–H species, providing a more complete mechanistic picture for this system. The active species, reaction mechanism, and the protonation sites on the $[Fe_4S_4]$ clusters were further confirmed by density functional theory calculations. The observed H-atom transfer reactivity of these coordination polymer-coated electrodes motivates additional applications of this composite material in reductive H-atom transfer electrocatalysis.

Introduction

Fe-S clusters are ubiquitous in nature due to their important functional roles, including electron transport, catalysis, sensing, and sulfur donation.[2-5] These clusters have prototypical reversible redox-chemistry which underpins many of these biological functions. In addition to this redox-chemistry, several studies suggest that Fe-S clusters can engage in H-atom or coupled proton-electron transfer (CPET) processes.[6-7] This broad range of useful reactivity in Fe-S clusters, in addition to their fundamentally interesting electronic structures, has motivated substantial efforts to develop synthetic analogues.[4, 8-12] In particular, cuboidal $[Fe_4S_4]$ clusters are one of the most abundant types of these compounds and are one of the most studied examples since the preparation of the first synthetic $[Fe_4S_4]$ cluster in the 1970s.[13-14] Most $[Fe_4S_4]$-based clusters share similar $[Fe_4S_4(SR)_4]^{2-}$ (SR = thiolate ligands) core structures, which mimic cysteine ligation in biology.

While the canonical reactivity of $[Fe_4S_4]$ clusters involves electron transfer, there are also some examples of these moieties serving as catalytic sites. For instance, synthetic $[Fe_4S_4]$ clusters were found to be active in electrocatalytic CO_2 reduction and both biogenic and synthetic $[Fe_4S_4]$ clusters catalyze the reduction of CO_2 to hydrocarbons although the speciation and mechanism of these systems is still an area of active investigation.[15-18] CPET reactivity is invoked in these reactions and reduced/protonated $[Fe_4S_4]$ intermediates have been proposed as an essential part of catalytic cycles. However, experimental results suggest that the protonation of $[Fe_4S_4(SR)_4]^{2-}$ may lead to the dissociation of thiolate ligands to form oxidized $[Fe_4S_4(SR)_3L]^{-}$ clusters (L = an external ligand such as acetonitrile).[19] Reduced protonated $[Fe_4S_4]$ species are not well characterized experimentally.[4] A key question is the protonation site on the $[Fe_4S_4]$ clusters, which could be on the Fe, a bridging sulfur in the cluster, or the sulfur in the thiolate ligands.

Recently, a soluble $[Fe_4S_4(SR)_4]^{2-}$ cluster, $[Fe_4S_4(SPh)_4][Et_4N]_2$ (**Fe_{sol}**, Et_4N = tetraethylammonium), was employed as a CPET mediator in electrocatalytic CO_2 reduction with a $Mn^I(bpy)(CO)_3Br$ (**1**, bpy = 2,2'-bipyridine) co-catalyst.[1] In contrast to the production of CO with **1** as the sole catalyst,[20] HCOOH was identified as the main product with **Fe_{sol}** acting as a CPET mediator. This dramatic selectivity change was attributed to CPET processes with

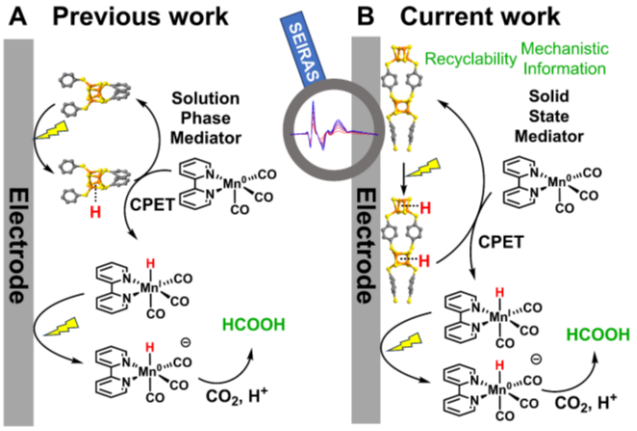

Figure 1. Schematic demonstration of Fe_4S_4-mediated CO_2 reduction in the (A) previous[1] and (B) current work.

reduced/protonated [Fe_4S_4] clusters as key intermediates (Fig. 1A). This finding adds to exciting recent reports of new reactivity enabled by other soluble CPET mediators.[21-30] Inspired by this work, we reasoned that developing solid-state CPET mediators for electrocatalytic processes would aid in recyclability, separation of desired solution-phase products, and potentially enhanced compatibility with different electrolytes or co-catalysts.

Several [Fe_4S_4] clusters have been embedded in polymeric supports such as polystyrene and cyclodextrins.[31-32] Graphene also supports [Fe_4S_4] clusters and the resultant composite materials show electrocatalytic hydrogen evolution activity.[33] Chalcogels composed of metal-sulfur clusters including [Fe_4S_4] clusters also serve as catalysts for several reductive processes.[34-36] Combining [Fe_4S_4] clusters and ditopic N-heterocyclic carbene linkers leads to amorphous conductive materials.[37] Our laboratory has also used [Fe_4S_4] clusters to design well-defined crystalline coordination polymers (CPs) with [Fe_4S_4] clusters and 1,4-benzenedithiolate (BDT).[38-39] Importantly, this 1D coordination polymer, [(Fe_4S_4)(BDT)$_2$][TMA]$_2$ (**Fe$_{CP}$**, TMA = tetramethylammonium), is soluble in dimethylformamide (DMF) which suggests that solution processing should be possible, for instance with drop-casting onto an electrode. As such, we targeted new heterogeneous CPET mediators with this material.

Here, we show that **Fe$_{CP}$** can serve as a highly active heterogeneous electrochemical CPET mediator (Fig. 1B). An ink of **Fe$_{CP}$** with polyvinylidene fluoride (PVDF) in DMF can be drop-cast onto glassy carbon (GC) electrodes. When combined with **1** as a co-catalyst, the resulting electrodes show high turnover numbers for CO_2 reduction with good selectivity for HCOOH. The **Fe$_{CP}$** coated electrodes also show good recyclability with no measurable drop in activity for HCOOH production over multiple catalytic trials. The heterogeneous nature of **Fe$_{CP}$** films enables surface-enhanced infrared absorption spectroscopy (SEIRAS) studies for *in-situ* analysis of interfacial structure during CO_2 reduction. Density functional theory (DFT) calculations elucidate the observed features from the SEIRAS experiments and provide insight into the mechanism of CO_2 reduction catalysis. These results demonstrate an important proof-of-concept for the heterogenization of soluble electrochemical CPET mediators, using [Fe_4S_4] clusters as a specific example, and motivate applications of these functionalized electrodes in a variety of reductive processes.

Results and Discussion

Deposition and Electrochemistry of ***Fe$_{CP}$***

The structure and electrochemical properties of **Fe$_{CP}$** have been previously reported.[38] This compound possesses a 1D structure and exhibits discrete redox events on the Fe_4S_4 clusters. Most importantly, **Fe$_{CP}$** is soluble in DMF, resulting in homogenous black solution, and hence **Fe$_{CP}$** was deposited on the surface of GC electrodes via drop-casting (see SI). The ink was a homogenous DMF solution of **Fe$_{CP}$** and PVDF. The use of PVDF as a binder is essential as films

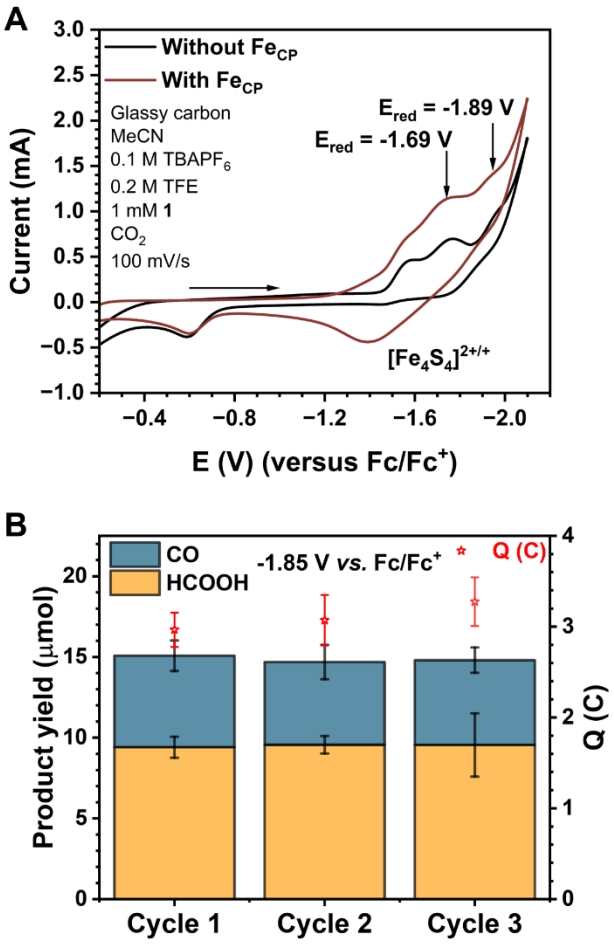

Figure 2. (A) Cyclic voltammogram traces of **1** in the absence (black curve) and in the presence (red curve) of **Fe$_{CP}$** on the surface of GC electrodes collected at 100 mV / s. (B) Reaction products (left axis) and total passed charge (Q, right axis) after 90 minutes of controlled potential electrolysis at -1.85 V versus Fc/Fc$^+$ for three sequential catalytic cycles conducted using the same **Fe$_{CP}$** coated GC electrode. In all experiments, the solution phase shares the same composition: 1mM **1**, 0.2 M TFE, 0.1 M $TBAPF_6$ in MeCN.

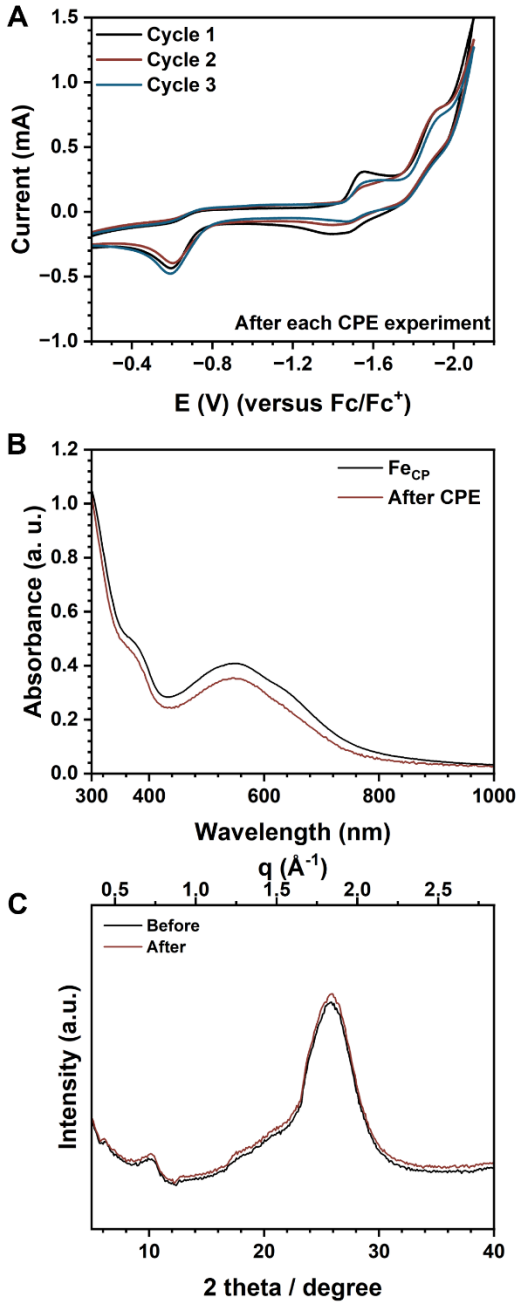

Figure 3. (A) Cyclic voltammogram traces after each controlled potential electrolysis (CPE) experiment on the same glassy carbon electrode. The solution phase composition: 1mM **1**, 0.2 M TFE, 0.1 M $TBAPF_6$ in MeCN. (B) UV-vis spectroscopy of the **Fe$_{CP}$** before and after CPE. The sample solution before CPE was prepared by dissolving fresh **Fe$_{CP}$** in DMF with ultrasonication. The sample solution after CPE was prepared by ultrasonicating the **Fe$_{CP}$** coated glassy carbon plate in DMF for 15 minutes. (C) One-dimensional scattering profiles obtained from the two-dimensional GIWAXS data on **Fe$_{CP}$** coated glassy carbon plate before and after CPE. Note that the broad peak at 25° can be assigned to glassy carbon.

of pure **Fe$_{CP}$** result in film flaking after electrochemical experiments. Pure PVDF was found to have minimal electrocatalytic activity (see Table S1). PVDF was ultimately the best binder for these studies as we observed that Nafion, as an alternative binder, dissolves during the electrochemical process. A grazing-incidence wide-angle X-ray scattering (GIWAXS) measurement on the film suggests that the deposited compounds are amorphous after the dissolution and deposition (Fig. S8). Finally, a mixture of **Fe$_{CP}$** and PVDF was deposited on the surface of the optical element of an attenuated total reflectance infrared spectrometer (ATR-IR). The recorded IR spectrum confirms the presence of both **Fe$_{CP}$** and PVDF (Fig. S9).

We then performed cyclic voltammetry (CV) to study the redox behavior of **Fe$_{CP}$** coated GC electrodes (Fig. S3). A broad reversible redox process can be observed at −1.4 V (all potentials quoted versus Fc/Fc$^+$) which can be assigned to a $[Fe_4S_4]^{2+/1+}$ redox process based on comparison to the literature.[1, 38] This redox process remains intact after several CV scans, indicating effective binding of the prepared films to the electrodes and good electrochemical reversibility (Fig. S3). The CV of an acetonitrile (MeCN) solution with **1**, 0.1 M $TBAPF_6$ electrolyte, **Fe$_{CP}$** coated GC as a working electrode, trifluoroethanol (TFE) as a proton donor, and CO_2 is shown in Fig. 2A. Three redox processes at −1.4, −1.69, and −1.89 V versus Fc/Fc$^+$ are observed. These features match well with the features observed for **Fe$_{sol}$** in the solution phase.[1] The two features at −1.69 and −1.89 V versus Fc/Fc$^+$ can be assigned to the reduction of **1** to $[Mn^0(bpy)(CO)_3L]$ (L = exogenous ligand such as MeCN) and $[Mn^0(bpy(CO)_3)^-$, respectively. A controlled CV experiment was also conducted on the same system with a bare uncoated GC electrode. The −1.4 V redox process from **Fe$_{CP}$** is absent, and the feature at −1.89 V also shows comparatively higher intensity demonstrating a different electrochemical process. Furthermore, a small feature at −0.6 V can also be observed, which is assigned to the oxidation to form $[Mn^I(bpy)(CO)_3]^+$ from $[Mn^0(bpy)(CO)_3]_2$ (**2**) which is formed from the one-electron reduction of **1**.[40] These results suggest that **Fe$_{CP}$** coated GC electrodes might be serving as CPET mediators in a similar fashion to the previously reported homogenous systems. To confirm that no soluble $[Fe_4S_4]$ species dissolve off the electrode, surface leaching tests were conducted (see SI). No features corresponding to $[Fe_4S_4]$ clusters can be observed in the CV and UV-vis spectrum after electrolysis at −1.85 V versus Fc/Fc$^+$ with **Fe$_{CP}$** coated glassy carbon electrodes (see below, and Fig. S7).

Electrocatalysis

We then performed controlled potential electrolyses (CPE) at −1.85 V for 90 minutes to test the activity of **1** for electrocatalytic CO_2 reduction with and without **Fe$_{CP}$** coated GC electrodes (Table S1) under conditions similar to the previous report (1 mM 1, 0.2 M TFE and 0,1 M $TBAPF_6$ in MeCN with CO_2 purged for 30 minutes prior to CPE). With **Fe$_{CP}$**, HCOOH was the dominant product with a Faradaic Yield (FY_{HCOOH}) of 61(4)%, and a FY_{CO} of 37(6)%. In contrast, GC electrodes without **Fe$_{CP}$** provide a FY_{CO} of 84(2)% with minimal HCOOH. These results confirm that the

heterogeneous **Fe$_{CP}$** coated electrodes play a similar role as homogeneous **Fe$_{sol}$**.

We note that the FY_{HCOOH} for **Fe$_{CP}$** coated electrodes is lower than the 90% reported for **Fe$_{sol}$**. This motivated us to perform several control experiments to elucidate the reaction parameters governing FY_{HCOOH} (Table S3). TFE concentration was initially varied. At a lower TFE concentration (0.1 M), a similar FY_{HCOOH} of 61.5% was observed, albeit with a slight reduction in the passed charge (from 2.83 to 2.32 C). At a higher TFE concentration (0.4 M), FY_{HCOOH} decreased to 52.3%, while the passed charge increased (to 3.34 C). Given that TFE is in excess in the reaction, a minimal change in FY_{HCOOH} might be expected with lower TFE concentrations. The decrease in FY_{HCOOH} at higher TFE concentrations is attributed to increased hydrogen evolution, as supported by previous studies.[1]

We also investigated the impact of varying the concentration of **1**. At a concentration of 0.5 mM, which is lower than the standard condition of 1 mM, we observe significantly reduced Faradaic yields for formic acid (FY_{HCOOH}, 39.0%) and carbon monoxide (FY_{CO}, 24.3%). Conversely, increasing the concentration of 1 to 2 mM resulted in enhanced FY_{HCOOH} (66.6%) and passed charge (3.68 C), indicating that higher concentrations of **1** are favorable for formic acid formation. This outcome was somewhat unexpected, since the amount of drop-cast **Fe$_{CP}$** contains many fewer [Fe_4S_4] clusters than comparable conditions with soluble **Fe$_{sol}$** due to the limited surface area of the GC electrode. The ratio of [Fe_4S_4]:**1** is 1:12 in the current systems, which is much lower than the value of 2 from the optimized catalytic conditions with **Fe$_{sol}$**. Previous reports have shown that decreasing the ratio of [Fe_4S_4]:**1** leads to lower FY_{HCOOH} due to reduced mediator concentration relative to the Mn catalyst. The increase in FY_{HCOOH} with higher concentrations of **1** in our system suggests that FY_{HCOOH} is influenced by the diffusion rate of **1** to the electrode surface. The diffusion of **1** to the **Fe$_{CP}$**/PVDF layer is confirmed by X-ray photoelectron spectroscopy (XPS). Mn signals were detected after CPE and significantly less Mn was observed after etching of the surface of the electrodes post CPE (Fig. S10 and S11, Table S4). The higher concentration of **1** likely leads to higher local concentrations of **1** at the electrode surface which results in better selectivity and activity. It is also noticeable that the turnover number (TON) for **1** with **Fe$_{CP}$** is 0.7, lower than the reported value of 2∼4 with **Fe$_{sol}$** in solution. However, the TON per [Fe_4S_4] cluster is 9 with **Fe$_{CP}$,** higher than the value of ∼2 with **Fe$_{sol}$** in solution. This observation may suggest that the heterogenization of the [Fe_4S_4] clusters on an electrode increases per-cluster activity. Similar activity enhancement has been observed in other heterogenized molecular electrocatalysts.[41]

To further investigate the influence of the ratio of [Fe_4S_4]:**1** on FY_{HCOOH}, we also modified the loading of **Fe$_{CP}$**. With 3 mg loading of **Fe$_{CP}$** (versus 6 mg in the standard conditions), a lower FY_{HCOOH} (42.4%) and a higher FY_{CO} (36.5%) were observed. This unsurprisingly suggests that the loading of **Fe$_{CP}$** significantly impacts the FY_{HCOOH}. A higher 10 mg loading of **Fe$_{CP}$** also results in a diminished FY_{HCOOH} (48%). Notably, more wrinkles can be observed on the surface of the electrode with 10 mg loading which suggests that the binder struggles to effectively adhere to the electrode surface at higher **Fe$_{CP}$** loadings and thus decreases FY_{HCOOH} (48%) due to background CO generation by the GC electrode. Thus, optimizing the **Fe$_{CP}$**:PVDF ratio is crucial to achieving a balance between high reaction activity and the mechanical stability of the films for recycling purposes.

We also varied the applied potential to assess this variable's effect on selectivity. At a more positive potential of −1.75 V versus Fc/Fc^+ we observed a decrease in FY_{HCOOH}. This decrease could be attributed to a slower generation of hydride species, which are crucial intermediates for formic acid generation. In contrast, when the potential is decreased to −1.95 V versus Fc/Fc^+, there is a slight decrease in FY_{HCOOH} to 60.6%. This observation aligns with studies involving molecular Fe_4S_4 clusters, suggesting that the increased hydrogen evolution at more negative potentials competes with the formation of formic acid, thus lowering the yield. These results underscore the delicate balance between optimizing electrochemical conditions and managing the competition between desired and undesired reactions.

Despite these control experiments, the origin of the lower FY_{HCOOH} with **Fe$_{CP}$** vs **Fe$_{sol}$** is still unclear. We propose that this may be primarily attributed to imperfect electrode coverage by films of **FeCP**. The drop-casting technique employed allows for the coating of only the two largest surfaces of the electrode, while the surface of the four small sides cannot be covered (Fig. S6). The bare GC surfaces are active only towards CO formation, which lowers the observed FY_{HCOOH}. Based on control experiments with and without a **Fe$_{CP}$** coating, the FY_{HCOOH} for **Fe$_{CP}$** coated electrodes can be estimated as ∼80% (see Section 2.2 in the SI).

The heterogenization of homogeneous catalysts has previously enabled catalyst recyclability.[42] We hypothesized that this advantage should also apply to heterogenized CPET mediators, so we tested the recyclability of **Fe$_{CP}$** coated electrodes. The same **Fe$_{CP}$** coated GC electrodes were used for electrocatalytic CO_2 reduction three times. Despite a slight swelling of the coated film after each experiment, only a slight drop in catalytic activity is observed (Fig. 2B, Table S2). The recyclability of **Fe$_{CP}$** is also supported by only slight changes in the CV post-electrolysis (Fig. 3A). Furthermore, the UV-vis spectra of re-dissolved **Fe$_{CP}$** films show an identical spectrum to as-synthesized **Fe$_{CP}$** (Fig. 3B). The GI-WAXS analysis of the film before and after electrolysis also confirms only minimal changes (Fig. 3C). Ex-situ XPS and scanning electron microscopy-energy dispersive X-ray analysis (SEM-EDX) results support a maintained 1:2 Fe:S after electrolysis (Table S4). The SEM results also show that the film remains smooth after CPE despite the formation of small wrinkles which are visible by eye (Fig. S5, S13). All of these data support the recyclability of the **Fe$_{CP}$** films over at least three cycles, and furthermore that the structure and composition of **Fe$_{CP}$** are preserved during and after electrocatalysis. As a final note, optical microscopy measurements suggest that the film thickness increases from 4 μm to 6 μm after electrolysis (Fig. S14). We tentatively assign this to ion exchange for larger TBA cations.

Mechanistic Studies

Previous research has studied the reaction mechanism of the $[Fe_4S_4]$ mediated electrocatalytic reduction of CO_2 with infrared spectro-electrochemistry and nuclear magnet resonance (NMR) spectroscopy.[1] We have employed NMR and infrared (IR) spectroscopy to study soluble intermediates or products in the current study. An *ex-situ* NMR spectrum of the reaction solution after 90 minutes of CPE is shown in Fig S1. Besides HCOOH, distinct resonances which can be assigned to the reduced Mn(0) dimer $[Mn^0(bpy)(CO)_3]_2$ (**2**) were observed as a major species, in addition to minor resonances for **1** and free bipyridine. Complex **2** arises from the reduction and dimerization of **1**.[20] The presence of **2** is also confirmed by *ex-situ* solution phase infrared spectroscopy, as shown in Fig. 4A.

With longer reaction times, the intensities of the IR features for **1** at 2028, 1932, and 1923 cm^{-1} decrease while the intensities for **2** at 1975, 1934, 1878, and 1853 cm^{-1} increase.[1] A feature for $[Mn^0(bpy)(CO)_3L]$ (**3**, L = exogenous ligand such as MeCN) at 2012 cm^{-1} can also be observed with a longer reaction time.[43] In the previous molecular study, the major Mn-based species observed in solution are $[Mn^I(bpy)(CO)_3H]$ (**4**) and **3**.[1] Interestingly, the features associated with **4** were not observed with $\mathbf{Fe_{CP}}$, which might be due to the instability of this species with *ex-situ* characterization techniques. However, the absence of **4** in both *ex-situ* NMR and IR spectroscopy measurements still suggests that heterogenization of the $[Fe_4S_4]$ clusters results in some mechanistic differences.

SEIRAS measurements were then conducted to probe how surface species differ from these bulk solution compounds under electrocatalytic conditions. This technique utilizes nanostructured electrode surfaces to amplify the signal of IR-active modes perpendicular to and within ~8 nm of the electrode/solution interface.[44] In contrast to glassy carbon, nanostructured Au is a common SEIRAS-active substrate,[45-46] but Au can also catalyze the

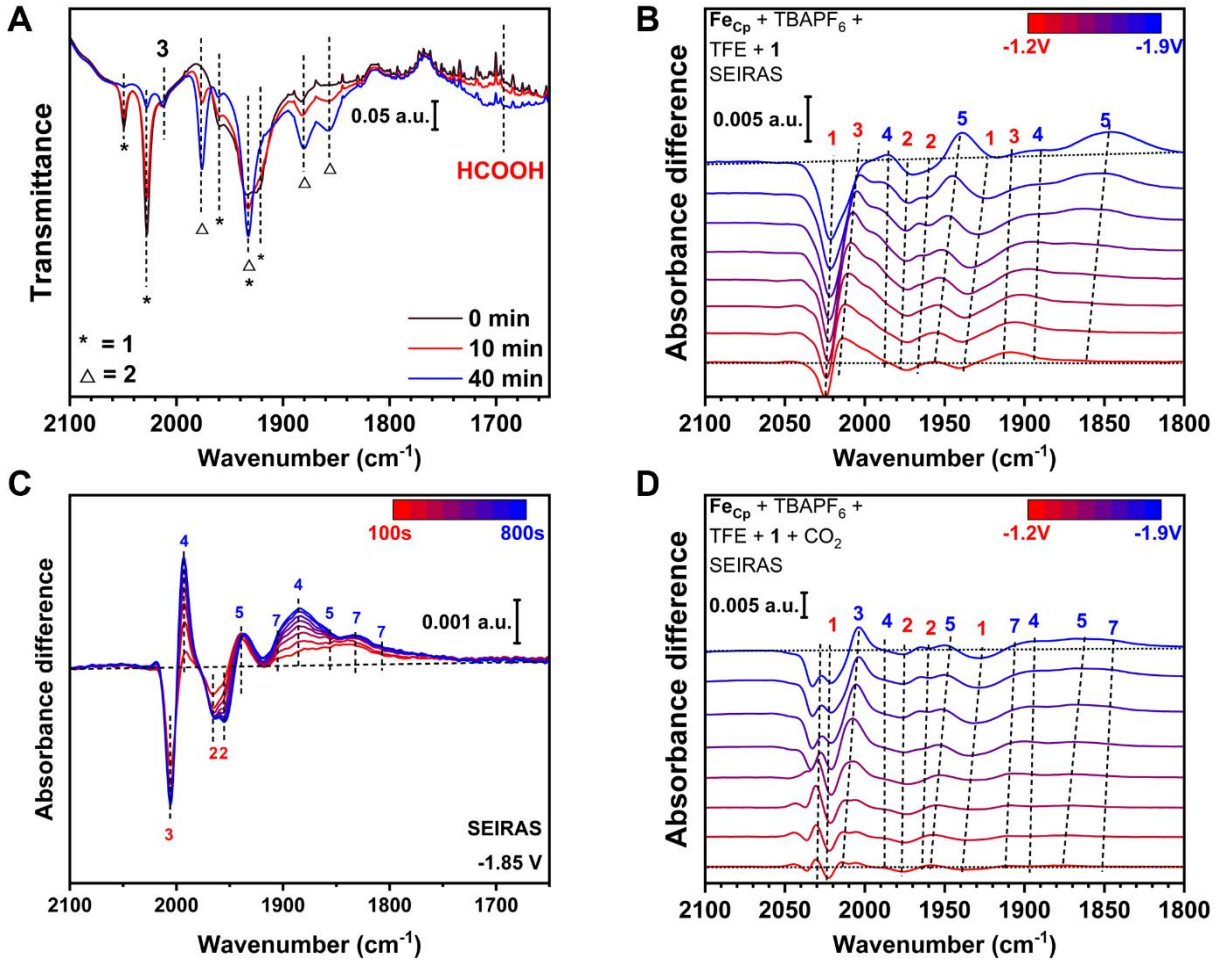

Figure 4. (A) *Ex-situ* solution phase IR spectra of reaction solution before CPE, after 10 minutes and 40 minutes of CPE. Surface-enhanced infrared absorption spectra of $\mathbf{Fe_{CP}}$ on Au surfaces (B) before CO_2 purge, and (D) after CO_2 purge after subtraction of background collected at -0.9 V under each condition. (C) Surface-enhanced infrared absorption spectra of $\mathbf{Fe_{CP}}$ on Au surfaces under CPE at –1.85 V versus Fc/Fc^+ from 100 s to 700 s after the subtraction of background collected after 30 s of electrolysis. In all SEIRAS experiments, 1 mM **1**, 0.2 M TFE, 0.1 M $TBAPF_6$ in MeCN were used. The $\mathbf{Fe_{CP}}$ was coated on the gold-coated Si prism.

electrochemical reduction of CO_2 in the aqueous phase.[47] Thus, we initially tested the CO_2 reduction activity of a pristine gold foil under our catalytic conditions as a control. Fortunately, only poor activity was observed (Table S1). With this control data, we then deposited a film of $\mathbf{Fe_{CP}}$ and PVDF on this gold electrode. The coated electrodes show good selectivity for HCOOH with FY_{HCOOH}= 72% under the same conditions as the coated GC electrodes. Good recyclability can also be observed with gold electrodes (Fig. S4). No film swelling was observed on gold, which could arise from better binding between gold and sulfur in $\mathbf{Fe_{CP}}$ (Fig. S5b). These control experiments suggest that gold can be used as a good surrogate for the previously measured GC electrodes. We therefore acquired SEIRAS data on films of $\mathbf{Fe_{CP}}$ deposited on a Au-coated silicon prism.

Background spectra were recorded at −0.9 V versus Fc/Fc^+ with and without a CO_2 purge. The background-subtracted SEIRA spectra are shown in Figs. 4B, 4D, and S15 – S18. Several features between 1800 cm^{-1} and 2100 cm^{-1} change with different applied potentials between −1.2 V to −1.9 V versus Fc/Fc^+ before and after CO_2 purge (Figs. 4B and 4D). These peaks can be assigned to CO vibrational modes from different Mn species by comparing experimental IR spectra with published results or DFT predictions (Table S5).[1, 48-49] It is notable that the vibrational frequencies from SEIRAS were measured under negative electric field and shifts of vibrational frequencies can be observed with changed applied potentials due to Stark effects. The shift of vibrational frequencies was also observed in recent SEIRA studies on related manganese carbonyl compounds.[49] All the following vibrational frequencies, if not specifically mentioned, refer to frequencies observed in spectra collected at −1.8 V versus Fc/Fc^+. The features at 2021, 1972, 1962 and 1926 cm^{-1} decrease with more negative potentials. The features at 2021, and 1926 cm^{-1} are assigned to **1**, while the 1972 and 1962 cm^{-1} features are assigned to **2**. In contrast, features at 2004, 1987, 1890, 1943 and 1851 cm^{-1} increase with more negative potentials suggesting a more reduced complex. Based on previous reports, the 2004 cm^{-1} feature can be assigned to mononuclear Mn(0) compound **3**, while the 1987 and 1890 cm^{-1} features are assigned to the Mn(I) hydride **4**.[50] Calculations support that the feature at 1943, and 1851 cm^{-1} can be assigned to an even more reduced $[Mn^0(bpy)(CO)_3H]^-$ (**5**) species (see Fig. S30). DFT calculations predict that the features of **5** should be located at 1972, 1880 and 1875 cm^{-1}. However, the features at 1943 and 1851 cm^{-1} (at −1.8 V versus Fc/Fc^+) show a distinctly larger shift at different applied potentials, suggesting that this species may be affected by a large Stark effect. Notably, the intensities of the features of **4** and **5** decreased after purging with CO_2 suggesting these hydride species are consumed under catalytic conditions. Finally, we also observe lower energy features at 1904 and 1832 cm^{-1} at potentials lower than −1.5 V (versus Fc/Fc^+). These features can be assigned to another negatively charged species, $[Mn^0(bpy)(CO)_3]^-$, **7**, since the reported carbonyl stretching frequencies for this species are 1911, 1837 and 1811 cm^{-1}.[51]

To further study the change of active species under electrocatalytic conditions, *in-situ* SEIRAS was also performed as shown in Fig. 4C and Fig. S19. These spectra were collected while a −1.85 V potential versus Fc/Fc^+ was applied to the same reaction solution (1 mM **1**, 0.1 M $TBAPF_6$ and 0.2 M TFE (non-deuterated trifluoroethanol) in MeCN solution) with a $\mathbf{Fe_{CP}}$/PVDF coated gold prism as working electrode after 30 minutes of CO_2 purge. As shown in Fig. 4C, features assigned to **2** and **3** decrease in intensity while features assigned to **4**, **5**, and **7** increase in intensity over 100-800s in the presence of TFE. These features are consistent with the conversion and accumulation of Mn–H species.

To further test the formation of Mn–H species, TFED (deuterated trifluoroethanol) was also used instead of TFE in *in-situ* SEIRAS experiments (Fig. S19). DFT calculations suggest that little to no change is expected in the ν_{CO} stretching frequencies upon deuteration (Fig. S27 to S32). This matches our observations as the features assigned to **4** and **5** are both observed in TFED experiments. Calculations also suggest the observation of a Mn–H feature at 1598 cm^{-1} for **4** and 1499 cm^{-1} for **5**, and a corresponding Mn–D feature at 1140 cm^{-1} for deuterated **4** and 1071 cm^{-1} for deuterated **5**. Several overlapping features between 1000-1200 cm^{-1} prevent the observation of any Mn–D signals, however the higher energy Mn–H region is more tractable (Fig. S19). Previous studies report TBA(HCOO) shows ν_{CO} features at 1608 cm^{-1}, and our data also show a signal at this energy with TFE.[1] With TFED, this feature shifts to 1590 cm^{-1} which we assign to the formation of $DCOO^-$. This result indicates that formate is initially formed at the electrode surface during electrocatalysis instead of formic acid which should appear at 1700 cm^{-1}. More interestingly, an apparent shoulder near the TBA(HCOO) feature and a more pronounced peak at 1500 cm^{-1} are observed for the TFE spectrum but not for the TFED spectrum. The diminishment of these features with deuteration suggests that they may be reasonably assigned as ν_{MnH} features arising from **4** and **5** respectively based on the abovementioned DFT predictions.

As a final note from the SEIRAS analysis, the observation of features for various $Mn(bpy)(CO)_3$ complexes implicates surface adsorption or association, as purely diffusive molecules at 1 mM concentration are not expected to show signals. [52] In addition, the observation of Stark effects further supports an interfacial structure in which the Mn species is adsorbed or associated with the electrified surface. Similar CVs between GC and Au SEIRAS experiments support similar adsorption or association between these two setups, however we cannot rule out the possibility of mechanistic differences arising from close association of the Mn co-catalysts between the two substrates.

The SEIRAS results were also used for examining possible $[Fe_4S_4]$-based active species, especially possible protonated/reduced intermediates. We initially performed DFT calculations to test possible protonation sites. These calculations suggest that the thiolate sites (*i.e.*, the sulfur atoms on the BDT ligands) are the most basic sites in $\mathbf{Fe_{CP}}$. Protonation on either sulfide or Fe in the $[Fe_4S_4]$ core leads to less stable isomers. We observe a small feature at 1640 cm^{-1} which, based on calculations, can be assigned to an aryl

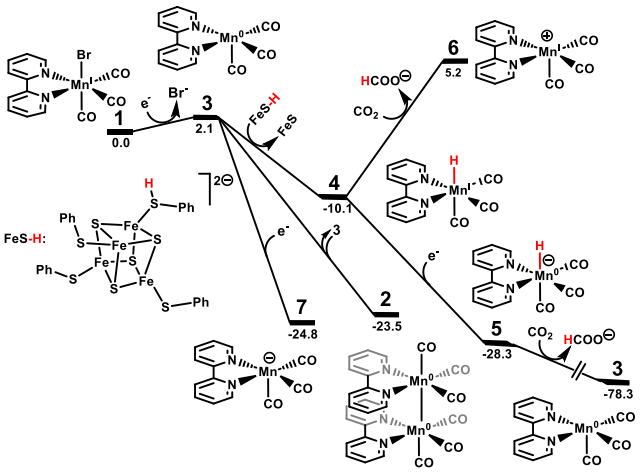

Figure 5. Free energy pathways calculated at TPSSh-D3BJ/Def2QZVP: Fe; Def2TZVP: all; SMD: ACN level of theory at T = 298 K. ΔG^0 values are in kcal/mol.

breathing mode of a $[Fe_4S_4BDT_2]H^{2-}$ species on the surface of the **Fe$_{CP}$** coated electrode (Fig. S18). Adding **1** depletes this feature, putatively via consumption of $[Fe_4S_4BDT_2]H^{2-}$ and formation of **4**. Theory demonstrates that the 1640 cm^{-1} mode is IR inactive in as-deposited **Fe$_{CP}$**, but it gains intensity as the symmetry decreases in the benzene substituents (see Section 5.2 in the SI), consistent with experiments. The observation of the 1640 cm^{-1} band in the experimental spectra after hydrogenation points towards a decreased symmetry of the phenyl substituents, as would be expected with protonation of one of the sulfur's of BDT. This supports the DFT results that indicate that the BDT linkers are the most stable protonation site in **Fe$_{CP}$** (Fig. S20). Although water has a possible convoluting active mode at ~1650 cm^{-1}, the infrared spectrum of the TFE used in the experiment as well as the electrolyte rules out the possibility of trace water (Fig. S9, S16, and S18). Clear features between 2400 cm^{-1} to 2700 cm^{-1} that might correspond to ν_{SH} were not observed in the SEIRAS experiments. The lack of S–H features can likely be attributed to the weak intensity of ν_{SH} as predicted by DFT. Still, the weak feature at 1640 cm^{-1}, only observed in the absence of **1**, may report on the spectroscopic data on a protonated/reduced cluster.

The sum of the NMR, solution phase IR, SEIRAS, and DFT data, combined with data from previous reports, allows us to propose the reaction mechanism shown in Fig. 5. We note that the electronic structures of iron-sulfur clusters are known to be very complicated. We used broken-symmetry DFT (BS-DFT) to accurately predict the protonation sites and electronic structure on $[Fe_4S_4]$, and our obtained results match closely with previous literature treatments of these fragments.[53-56] We also calculated the free energies of the proposed reaction mechanism with DFT using molecular $[Fe_4S_4]^{2+}$ clusters ("**FeS**") as proxies for **Fe$_{CP}$** (Fig. 5). The reaction starts with the $Mn^{I}Br$ species **1** as the pre-catalyst of the reaction which is electrochemically reduced to **3** in a slightly endergonic step of 2.1 kcal/mol. In a parallel reaction, **FeS-H** is also formed by cluster reduction and protonation of one of the bound thiophenolate moieties.

After the formation of **3** and **FeS-H**, the reaction trifurcates following three separate pathways: (i) dimerization of **3** to **2**; (ii) electrochemical reduction of **3** to form **7**; (iii) CPET from **FeS-H** to **3** to generate **4** and productive reactivity. The dimerization to generate **2** is exergonic at −23.5 kcal/mol; this step is most likely to take place with a comparatively high concentration of **3** or low concentration of **FeS-H**. Similarly, the reduction of species **3** to form **7** likely occurs through contact with the bare electrode which is uncovered by the **FeS-H** substrate. Finally, **FeS-H** can react with **3** to access the productive pathway where a hydrogen atom is transferred to **3** to generate **4** in an exergonic step of −12.2 kcal/mol. This latter step is comparatively favored over dimerization or further reduction due to the high local concentration of **FeS-H**, and the slightly endergonic formation of species **3** that keeps this intermediate in low concentration. We calculate that the Mn–H bond dissociation free energy (BDFE) of **4** is 52.1 kcal/mol, which therefore implies a computed FeS–H BDFE in **FeS-H** of 47.5 kcal/mol. This weak predicted BDFE of the protonated $[Fe_4S_4]$ cluster supports its proposed activity as a CPET mediator. We also calculate that **4** can then be further electrochemically reduced to **5**. This step is exergonic with a free energy change of −8.2 kcal/mol. Complex **5** can then react with CO_2, leading to the formation of TBA(HCOO) and **3** in solution. This final step is irreversible with −50.0 kcal/mol in free energy change. TBA(HCOO) then putatively diffuses to the solution phase and gets protonated to form HCOOH. This proposed mechanism matches well with the previous report on the **Fe$_{sol}$** system, although we see additional intermediates due to the ancillary spectroscopic methods utilized here.[1] The formation of **2** and **7** might be responsible for the observation of a large amount of CO and a lower per Mn TON in the heterogeneous system compared to the homogeneous system since **7** has been proposed to be responsible for the generation of CO during CO_2 reduction reactions.[57] As mentioned, we hypothesize that the reduction from **2** to **7** likely takes place on uncoated GC.

Conclusion

We report how a solution-processable $[Fe_4S_4]$-based CP can be successfully deposited on the surface of GC and Au electrodes. These coated electrodes have high Faradaic Yields for HCOOH generation from CO_2 with a soluble Mn co-catalyst, in line with recent studies on a homogeneous system. Electrocatalytic activity and selectivity were maintained over multiple cycles which suggests good recyclability of the **Fe$_{CP}$** coated electrodes. The major equilibrium catalyst speciation was probed by both *ex-situ* solution-phase IR and *in-situ* SEIRAS methods. The data are consistent with an active Mn–H species that is produced on the electrode surface by a CPET process with a $[Fe_4S_4]$ cluster as a mediator, followed by diffusion and HCOOH formation in the bulk solution. While no direct S–H features for the active CPET mediating intermediate were observed in the SEIRAS data, DFT calculations suggest that a weak feature at 1640 cm^{-1} may be a spectroscopic signature of protonated/reduced $[Fe_4S_4]$ clusters.

The results presented here support that $[Fe_4S_4]$ clusters embedded in CPs can still serve as heterogeneous CPET mediators. In contrast to previous reports that have used $[Fe_4S_4]$ clusters as direct catalysts, where the speciation and stability of the cluster catalyst can be unclear or challenging to characterize, this work demonstrates how heterogenized Fe-S based materials can serve as robust, recyclable, and highly active co-catalysts with molecular species. This suggests exciting applications of these coated electrodes with a wide range of molecular catalysts for reductive transformations.

Experimental Section

General Methods. All manipulations were performed under dry N_2 using MBraun UNIlab glovebox unless otherwise noted. Glassware was dried at 180 °C for overnight and cooled under vacuum prior to use. The acetonitrile (MeCN) and dimethylformamide (DMF) were initially dried and purged with N_2 on a solvent purification system from Pure Process Technology. MeCN and DMF were then passed through activated alumina and stored over 4 Å molecular sieves. $[(Fe_4S_4)(BDT)_2][TMA]_2$ (**Fe$_{CP}$**) and $bpyMn(CO)_3Br$ (**1**) (BDT = 1,4-benzenedithiolate, TMA = tetramethylammonium and bpy = bipyridine) were synthesized as previously described.[20, 38] All other chemicals were purchased from commercial sources and used as received unless noted. The trifluoroethanol (TFE) was purged with N_2 for 30 minutes before being transferred into the glovebox.

Preparation of working electrode. 1 cm * 1 cm * 0.15 cm glassy carbon plates and a piece of thin gold foil (a 0.8 cm * 1.0 cm area was coated with **Fe$_{CP}$**) were used as working electrodes in the experiment. The glassy carbon and the gold electrode were ultrasonicated in DMF for 5 minutes to remove any residual impurities. Then, the glassy carbon electrodes were polished on a cloth polishing pad in a water-alumina slurry. The gold electrode was cleaned by applying a potential from 0.2 V to 1.5 V versus $Ag/AgNO_3$ reference electrode (0.01 M) for five cycles with 50 mV/s scan rates in 0.1 M H_2SO_4 solutions. Both electrodes were ultrasonicated in isopropanol for 15 minutes and dried in air.

A mixture of polyvinylidene fluoride (PVDF) and DMF was heated at 60 °C overnight with constant stirring. The complete dissolution of PVDF results in a DMF solution with a PVDF concentration of 10 mg/mL. Once cooled to room-temperature, 6 mg of **Fe$_{CP}$** was added to 1 mL of PVDF solution in a 23 mL glass vial. This vial was sealed with electrical tabe and was transferred outside the glovebox and ultrasonicated for 30 minutes, which allowed the dissolution of **Fe$_{CP}$** in the PVDF solutions. This as-prepared **Fe$_{CP}$** solution was transferred back into the glovebox as a stock solution. For glassy carbon plates, 50 µL of the stock **Fe$_{CP}$** solution was drop cast on each side of the glassy carbon plate and dried in the glovebox at room temperature for 4 hours. For the gold foil, 20 µL of **Fe$_{CP}$** stock solution was drop cast on each side of the foil and dried in the glovebox at room temperature for 6 hours. For one coated glassy carbon plate, 0.6 mg of **Fe$_{CP}$** was deposited on the surface of the electrode. The images of coated glassy carbon and gold electrodes can be found in Fig. S5.

Electrochemical studies. Electrochemical measurements were performed using a BAS Epsilon potentiostat and BAS Epsilon software version 1.40.67NT.

All the electrochemical experiments were performed in a custom-made airtight two-chamber H-cell with a pressure-equalizing arm separated by a fine glass frit. A platinum mesh was used as the counter electrode and placed in the anodic compartment. A glassy carbon plate or gold electrode (described in the previous section) was used as the working electrode in the cathodic compartment. The carbon or gold electrode was clamped by a steel toothless alligator clip with smooth jaws, and the clip was attached to a piece of copper wire connected to the potentiostat. When a glassy carbon plate was used as a working electrode, 80% of the electrode was submerged into the solution to avoid direct contact between the steel clip and the solution. An Ag^+/Ag (0.01 M $AgNO_3$ + 0.1 M $[^nBu_4N]PF_6$ in MeCN) was used as a reference electrode in the cathodic compartment. In all electrochemical studies, 0.1 M $[^nBu_4N]PF_6$ ($TBAPF_6$) was used as a supporting electrolyte. The acetonitrile was used as solvent for all experiments. The H-cell was covered by aluminum foil to protect the active species (the Mn carbonyl species) from degradation.

Cyclic voltammetry. The cyclic voltammetry experiments were performed in a custom-made H-cell. The assembly of the H-cell was described in the previous section. A 1 mM concentration of **1** and 0.2 M of TFE in the cathodic chamber were used for CV measurements. All potentials were referenced to an internal Fc/Fc^+ standard added in the last step of each experiment. For irreversible processes, the potential at which half of the peak current ($I_c/2$) is reached has been considered the half-wave potential ($E_{1/2}$). The scan rate was 100 mV/s unless otherwise noted.

Controlled potential electrolysis. After assembling the H-cell in the glovebox, the cell was transferred outside the box. The cell was purged with CO_2 for at least 30 minutes before the CPE. Constant magnetic stirring of 400 rpm with a small stir bar was applied during the electrolysis. A 1 mM concentration of **1** and 0.2 M of TFE in the cathodic chamber were used for all CPEs. Product detection was specified in detail in the SI. Previously, the charge required to reduce to Mn(0) was subtracted from the total charge passed. In our experiment this subtraction should be 0.87 C as the ratio of **1**: **Fe$_{CP}$** is 12:1 which is significantly higher than the reported homogeneous conditions (1:3 ~ 1:1).

Computational methods

Periodic density functional theory (DFT) calculations were performed on a single unit cell of each considered species using the Vienna Ab Initio Simulation Package (VASP 6.4.0).[58] The Perdew-Burke-Ernzerhof (PBE) exchange-correlation density functional was used along with Grimme's D3 dispersion correction with Becke-Johnson damping (D3BJ).[59-60] As a correction to the PBE functional, the Coulomb and exchange interactions of the localized d-orbitals in Fe centers were treated within the framework using the DFT + U method. [61] The effective Coulomb (U) and exchange (J) parameters were set at U = 4 eV and J = 0 eV. A plane-wave basis set with a kinetic energy cut-off of 520 eV was used for the geometry optimizations, and normal

pseudopotential for all atoms. Energy and force convergence criteria of 10^{-6} eV and 0.01 eV $Å^{-1}$, respectively, were employed for all optimizations. Due to the modestly large size of the unit cell, a 3 × 3 × 1 and a 2 × 2 × 1, a Γ-centered k-point grid was used for the Brillouin zone sampling for the polymer with ^{+}Li and $^{+}NMe_4$ counterion, respectively. Single-point calculations were performed using the functionals SCAN,[62] including D3BJ dispersion correction. A plane-wave basis set with a kinetic energy cut-off of 910 eV was used and a hard pseudopotential for all atoms, and energy convergence criterion of 10^{-8} eV.

Molecular calculations were performed using Kohn Sham density functional theory (KS-DFT) with Gaussian 16 rev B01.[63] Geometry optimization was performed employing the hybrid functional TPSSh including the empirical dispersion correction with Becke and Johnson damping function D3BJ.[63] The Ahlrichs basis set def2-SVP[64] was used for geometry optimization for all atoms. The electronic energies were calculated by single point calculations, including the dispersion correction (D3BJ), at the B3LYP,[65-66] TPSSh,[59-60] and MN15[67] functionals, the latter without including the dispersion correction. As basis set def2-QZVP[64] for Fe and Mn, def2-TZVP[64] (**BBS**). Vibrational frequency calculation at 298 K was done at the optimization level of theory and used to define the nature of the stationary points involved in the reaction mechanism. The free energy correction applied to the electronic energy was calculated based on the frequency calculation setting a cut-off for small vibration to 100 cm^{-1}.[68] In addition, we used the solution phase standard state of 1 mol/l instead of the gas phase 1 atm used by default in Gaussian. The presence of the MeCN solvent has also been considered implicitly with the continuum solvent model SMD.[69]

ASSOCIATED CONTENT

Electrochemistry, product detection, structural and spectroscopy characterization, and DFT (PDF). Cartesian coordinates for the all the optimized geometries (ZIP).
This material is available free of charge via the Internet at http://pubs.acs.org.

AUTHOR INFORMATION

Corresponding Author

John S. Anderson − Department of Chemistry, University of Chicago, Chicago, Illinois 60637, United States ;
orcid.org/0000-0002−0730-3018; Email: jsanderson@uchicago.edu

Author

Ningxin Jiang - Department of Chemistry, University of Chicago, Chicago, Illinois 60637, United States ;
Andrea Darù - Department of Chemistry, University of Chicago, Chicago, Illinois 60637, United States ;
Špela Kunstelj - Department of Chemistry, University of Chicago, Chicago, Illinois 60637, United States ;
Jenny G. Vitillo - Department of Science and High Technology and INSTM, Università degli Studi dell'Insubria, Como, 22100, Italy
Maia E. Czaikowski - Department of Chemistry, University of Chicago, Chicago, Illinois 60637, United States ;
Alexander S. Filatov - Department of Chemistry, University of Chicago, Chicago, Illinois 60637, United States ;
Anna Wuttig - Department of Chemistry, University of Chicago, Chicago, Illinois 60637, United States ;
Laura Gagliardi - Department of Chemistry, Pritzker School of Molecular Engineering, James Franck Institute, University of Chicago, Chicago, Illinois 60637, United States ;

Notes

The authors declare no competing financial interest.

ACKNOWLEDGMENT

This research was supported by the Catalyst Design for Decarbonization Center an Energy Frontier Research Center funded by the U.S. Department of Energy, Office of Science, Basic Energy Sciences under Award No. DE-SC0023383. This work made use of the shared facilities at the University of Chicago Materials Research Science and Engineering Center, supported by the National Science Foundation under Award DMR-2011854. We acknowledge the University of Chicago's Research Computing Center for providing the resources to carry out this work. We also thank Dr. Jorge Martinez for suggestions on electrochemistry, Dr. Patrick Crossland for optical microscopy measurements and Di Wang for SEM-EDX measurements.

REFERENCE

1. Dey, S.; Masero, F.; Brack, E.; Fontecave, M.; Mougel, V., Electrocatalytic metal hydride generation using CPET mediators. *Nature* **2022,** *607* (7919), 499-506.
2. Boncella, A. E.; Sabo, E. T.; Santore, R. M.; Carter, J.; Whalen, J.; Hudspeth, J. D.; Morrison, C. N., The expanding utility of iron-sulfur clusters: Their functional roles in biology, synthetic small molecules, maquettes and artificial proteins, biomimetic materials, and therapeutic strategies. *Coord. Chem. Rev.* **2022,** *453*, 214229.
3. Johnson, D. C.; Dean, D. R.; Smith, A. D.; Johnson, M. K., Structure, function, and formation of biological iron-sulfur clusters. *Annu. Rev. Biochem.* **2005,** *74*, 247-281.
4. Waser, V.; Ward, T. R., Aqueous stability and redox chemistry of synthetic [Fe_4S_4] clusters. *Coord. Chem. Rev.* **2023,** *495*, 215377.
5. Beinert, H.; Holm, R. H.; Munck, E., Iron-sulfur clusters: nature's modular, multipurpose structures. *Science* **1997,** *277* (5326), 653-659.
6. Warren, J. J.; Mayer, J. M., Moving protons and electrons in biomimetic systems. *Biochem.* **2015,** *54* (10), 1863-1878.
7. Bergner, M.; Dechert, S.; Demeshko, S.; Kupper, C.; Mayer, J. M.; Meyer, F., Model of the MitoNEET [2Fe-2S] cluster shows proton coupled electron transfer. *J. Am. Chem. Soc.* **2017,** *139* (2), 701-707.
8. Brown, A. C.; Suess, D. L., Synthetic Iron-Sulfur Clusters. **2021**.
9. Venkateswara Rao, P.; Holm, R., Synthetic analogues of the active sites of iron− sulfur proteins. *Chem. Rev.* **2004,** *104* (2), 527-560.
10. Badding, E. D.; Srisantitham, S.; Lukoyanov, D. A.; Hoffman, B. M.; Suess, D. L., Connecting the geometric and electronic structures of the nitrogenase iron−molybdenum cofactor through site-selective ^{57}Fe labelling. *Nat. Chem.* **2023,** *15* (5), 658-665.
11. McSkimming, A.; Suess, D. L., Dinitrogen binding and activation at a molybdenum−iron−sulfur cluster. *Nat. Chem.* **2021,** *13* (7), 666-670.

12. Grunwald, L.; Clémancey, M.; Klose, D.; Dubois, L.; Gambarelli, S.; Jeschke, G.; Wörle, M.; Blondin, G.; Mougel, V., A complete biomimetic iron-sulfur cubane redox series. *Proc. Natl. Acad. Sci. U.S.A.* **2022,** *119* (31), e2122677119.
13. Herskovitz, T.; Averill, B.; Holm, R.; Ibers, J. A.; Phillips, W.; Weiher, J., Structure and properties of a synthetic analogue of bacterial iron-sulfur proteins. *Proc. Natl. Acad. Sci. U.S.A.* **1972,** *69* (9), 2437-2441.
14. Averill, B.; Herskovitz, T.; Holm, R.; Ibers, J. A., Synthetic analogs of the active sites of iron-sulfur proteins. II. Synthesis and structure of the tetra [mercapto-.mu.3-sulfido-iron] clusters,$[Fe_4S_4(SR)_4]_2$. *J. Am. Chem. Soc.* **1973,** *95* (11), 3523-3534.
15. Tezuka, M.; Yajima, T.; Tsuchiya, A.; Matsumoto, Y.; Uchida, Y.; Hidai, M., Electroreduction of carbon dioxide catalyzed by iron-sulfur cluster compounds $[Fe_4S_4(SR)_4]_2$. *J. Am. Chem. Soc.* **1982,** *104* (24), 6834-6836.
16. Stiebritz, M. T.; Hiller, C. J.; Sickerman, N. S.; Lee, C. C.; Tanifuji, K.; Ohki, Y.; Hu, Y., Ambient conversion of CO_2 to hydrocarbons by biogenic and synthetic $[Fe_4S_4]$ clusters. *Nat. Catal.* **2018,** *1* (6), 444-451.
17. Lee, C. C.; Stiebritz, M. T.; Hu, Y., Reactivity of $[Fe_4S_4]$ clusters toward C1 substrates: Mechanism, implications, and potential applications. *Acc. Chem. Res.* **2019,** *52* (5), 1168-1176.
18. Nakazawa, M.; Mizobe, Y.; Matsumoto, Y.; Uchida, Y.; Tezuka, M.; Hidai, M., Electrochemical reduction of carbon dioxide using iron–sulfur clusters as catalyst precursors. *Bull. Chem. Soc. Jpn.* **1986,** *59* (3), 809-814.
19. Saouma, C. T.; Morris, W. D.; Darcy, J. W.; Mayer, J. M., Protonation and Proton - Coupled Electron Transfer at S - Ligated [4Fe - 4S] Clusters. *Chem. Eur. J.* **2015,** *21* (25), 9256-9260.
20. Bourrez, M.; Molton, F.; Chardon - Noblat, S.; Deronzier, A., [Mn (bipyridyl)$(CO)_3$Br]: an abundant metal carbonyl complex as efficient electrocatalyst for CO_2 reduction. *Angew. Chem. Int. Ed.* **2011,** *50* (42), 9903-9906.
21. Costentin, C.; Robert, M.; Savéant, J.-M., Concerted proton– electron transfers: Electrochemical and related approaches. *Acc. Chem. Res.* **2010,** *43* (7), 1019-1029.
22. Chalkley, M. J.; Garrido-Barros, P.; Peters, J. C., A molecular mediator for reductive concerted proton-electron transfers via electrocatalysis. *Science* **2020,** *369* (6505), 850-854.
23. Badalyan, A.; Stahl, S. S., Cooperative electrocatalytic alcohol oxidation with electron-proton-transfer mediators. *Nature* **2016,** *535* (7612), 406-410.
24. Galvin, C. M.; Waymouth, R. M., Electron-rich phenoxyl mediators improve thermodynamic performance of electrocatalytic alcohol oxidation with an iridium pincer complex. *J. Am. Chem. Soc.* **2020,** *142* (45), 19368-19378.
25. Derosa, J.; Garrido-Barros, P.; Li, M.; Peters, J. C., Use of a PCET Mediator Enables a Ni-HER Electrocatalyst to Act as a Hydride Delivery Agent. *J. Am. Chem. Soc.* **2022,** *144* (43), 20118-20125.
26. Garrido-Barros, P.; Derosa, J.; Chalkley, M. J.; Peters, J. C., Tandem electrocatalytic N_2 fixation via proton-coupled electron transfer. *Nature* **2022,** *609* (7925), 71-76.
27. Derosa, J.; Garrido-Barros, P.; Peters, J. C., Electrocatalytic reduction of C–C π-bonds via a cobaltocene-derived concerted proton–electron transfer mediator: fumarate hydrogenation as a model study. *J. Am. Chem. Soc.* **2021,** *143* (25), 9303-9307.
28. Warren, J. J.; Tronic, T. A.; Mayer, J. M., Thermochemistry of proton-coupled electron transfer reagents and its implications. *Chem. Rev.* **2010,** *110* (12), 6961-7001.
29. Agarwal, R. G.; Coste, S. C.; Groff, B. D.; Heuer, A. M.; Noh, H.; Parada, G. A.; Wise, C. F.; Nichols, E. M.; Warren, J. J.; Mayer, J. M., Free energies of proton-coupled electron transfer reagents and their applications. *Chem. Rev.* **2021,** *122* (1), 1-49.
30. Reid, A. G.; Machan, C. W., Redox Mediators in Homogeneous Co-electrocatalysis. *J. Am. Chem. Soc.* **2023,** *145* (4), 2013-2027.
31. Ueyama, N.; Oku, H.; Nakamura, A., Two-electron-transfer oxidation by polymer-supported $[Fe_4S_4(SR)_4]^{2-}$ complex. *J. Mol. Catal.* **1992,** *74* (1-3), 451-458.
32. Kuroda, Y.; Sasaki, Y.; Shiroiwa, Y.; Tabushi, I., Cyclodextrin sandwiched Fe_4S_4 cluster. *J. Am. Chem. Soc.* **1988,** *110* (12), 4049-4050.
33. Begum, A.; Sheikh, A. H.; Moula, G.; Sarkar, S., Fe_4S_4 cubane type cluster immobilized on a graphene support: a high performance H_2 evolution catalysis in acidic water. *Sci. Rep.* **2017,** *7* (1), 16948.
34. Yuhas, B. D.; Prasittichai, C.; Hupp, J. T.; Kanatzidis, M. G., Enhanced electrocatalytic reduction of CO_2 with ternary Ni-Fe_4S_4 and Co-Fe_4S_4-based biomimetic chalcogels. *J. Am. Chem. Soc.* **2011,** *133* (40), 15854-15857.
35. Shim, Y.; Young, R. M.; Douvalis, A. P.; Dyar, S. M.; Yuhas, B. D.; Bakas, T.; Wasielewski, M. R.; Kanatzidis, M. G., Enhanced photochemical hydrogen evolution from Fe_4S_4-based biomimetic chalcogels containing M^{2+} (M= Pt, Zn, Co, Ni, Sn) centers. *J. Am. Chem. Soc.* **2014,** *136* (38), 13371-13380.
36. Shim, Y.; Yuhas, B. D.; Dyar, S. M.; Smeigh, A. L.; Douvalis, A. P.; Wasielewski, M. R.; Kanatzidis, M. G., Tunable Biomimetic Chalcogels with Fe_4S_4 Cores and $[Sn_nS_{2n+2}]^{4-}$(n= 1, 2, 4) Building Blocks for Solar Fuel Catalysis. *J. Am. Chem. Soc.* **2013,** *135* (6), 2330-2337.
37. Kadota, K.; Chen, T.; Gormley, E. L.; Hendon, C. H.; Dincă, M.; Brozek, C. K., Electrically conductive $[Fe_4S_4]^-$based organometallic polymers. *Chem. Sci.* **2023,** *14* (41), 11410-11416.
38. Horwitz, N. E.; Xie, J.; Filatov, A. S.; Papoular, R. J.; Sheppard, W. E.; Zee, D. Z.; Grahn, M. P.; Gilder, C.; Anderson, J. S., Redox-active 1D coordination polymers of iron–sulfur clusters. *J. Am. Chem. Soc.* **2019,** *141* (9), 3940-3951.
39. Salinas, O.; Xie, J.; Papoular, R. J.; Horwitz, N. E.; Elkaim, E.; Filatov, A. S.; Anderson, J. S., Steric and electronic effects of ligand substitution on redox-active Fe_4S_4-based coordination polymers. *Dalton Trans.* **2021,** *50* (31), 10798-10805.
40. Hartl, F.; Rossenaar, B. D.; Stor, G. J.; Stufkens, D. J., Role of an electron - transfer chain reaction in the unusual photochemical formation of five - coordinated anions $[Mn(CO)_3(\alpha$ -diimine)- from fac - $[Mn(X)(CO)_3(\alpha$ -diimine)](X= halide) at low temperatures. *Recueil des Travaux Chimiques des Pays - Bas* **1995,** *114* (11 - 12), 565-570.
41. Wang, J.; Huang, X.; Xi, S.; Lee, J. M.; Wang, C.; Du, Y.; Wang, X., Linkage effect in the heterogenization of cobalt complexes by doped graphene for electrocatalytic CO_2 reduction. *Angew. Chem. Int. Ed.* **2019,** *58* (38), 13532-13539.
42. Petrucci, M. G.; Kakkar, A. K., Heterogenizing homogeneous catalysis. *Adv. Mater.* **1996,** *8* (3), 251-253.
43. Franco, F.; Cometto, C.; Nencini, L.; Barolo, C.; Sordello, F.; Minero, C.; Fiedler, J.; Robert, M.; Gobetto, R.; Nervi, C., Local proton source in electrocatalytic CO_2 reduction with $[Mn(bpy\text{-}R)(CO)_3Br]$ complexes. *Chem. Eur. J.* **2017,** *23* (20), 4782-4793.
44. Osawa, M., Dynamic processes in electrochemical reactions studied by surface-enhanced infrared absorption spectroscopy (SEIRAS). *Bull. Chem. Soc. Jpn.* **1997,** *70* (12), 2861-2880.
45. Wang, H.-L.; You, E.-M.; Panneerselvam, R.; Ding, S.-Y.; Tian, Z.-Q., Advances of surface-enhanced Raman and IR spectroscopies: from nano/microstructures to macro-optical design. *Light Sci. Appl.* **2021,** *10* (1), 161.
46. Aroca, R. F.; Ross, D. J.; Domingo, C., Surface-enhanced infrared spectroscopy. *Appl. Spectmsc.* **2004,** *58* (11), 324A-338A.
47. Wuttig, A.; Yaguchi, M.; Motobayashi, K.; Osawa, M.; Surendranath, Y., Inhibited proton transfer enhances Au-catalyzed

CO2-to-fuels selectivity. *Proc. Natl. Acad. Sci. U.S.A.* **2016,** *113* (32), E4585-E4593.
48. Reuillard, B.; Ly, K. H.; Rosser, T. E.; Kuehnel, M. F.; Zebger, I.; Reisner, E., Tuning product selectivity for aqueous CO2 reduction with a Mn (bipyridine)-pyrene catalyst immobilized on a carbon nanotube electrode. *J. Am. Chem. Soc.* **2017,** *139* (41), 14425-14435.
49. Singh, K. K.; Gerke, C. S.; Saund, S. S.; Zito, A. M.; Siegler, M. A.; Thoi, V. S., CO_2 Activation with Manganese Tricarbonyl Complexes by an H^- Atom Responsive Benzimidazole Ligand. *Chem. Eur. J.* **2023**, e202300796.
50. Rønne, M. H.; Cho, D.; Madsen, M. R.; Jakobsen, J. B.; Eom, S.; Escoudé, E. m.; Hammershøj, H. C. D.; Nielsen, D. U.; Pedersen, S. U.; Baik, M.-H., Ligand-controlled product selectivity in electrochemical carbon dioxide reduction using manganese bipyridine catalysts. *J. Am. Chem. Soc.* **2020,** *142* (9), 4265-4275.
51. Machan, C. W.; Stanton III, C. J.; Vandezande, J. E.; Majetich, G. F.; Schaefer III, H. F.; Kubiak, C. P.; Agarwal, J., Electrocatalytic reduction of carbon dioxide by Mn(CN)(2, 2′-bipyridine)$(CO)_3$:CN coordination alters mechanism. *Inorg. Chem.* **2015,** *54* (17), 8849-8856.
52. Badgurjar, D.; Huynh, M.; Masters, B.; Wuttig, A., Non-Covalent Interactions Mimic the Covalent: An Electrode-Orthogonal Self-Assembled Layer. *J. Am. Chem. Soc.* **2023,** *145* (32), 17734-17745.
53. Darù, A.; Martín-Fernández, C.; Harvey, J. N., Iron-Catalyzed Kumada Cross-Coupling Reaction Involving Fe_8Me_{12}–and Related Clusters: A Computational Study. *ACS Catal.* **2022,** *12* (20), 12678-12688.
54. Jimenez-Izal, E.; Alexandrova, A. N., Computational design of clusters for catalysis. *Annu. Rev. Phys. Chem.* **2018,** *69*, 377-400.
55. Ammal, S. C.; Yoshikai, N.; Inada, Y.; Nishibayashi, Y.; Nakamura, E., Synergistic dimetallic effects in propargylic substitution reaction catalyzed by thiolate-bridged diruthenium complex. *J. Am. Chem. Soc.* **2005,** *127* (26), 9428-9438.
56. Vajda, S.; Pellin, M. J.; Greeley, J. P.; Marshall, C. L.; Curtiss, L. A.; Ballentine, G. A.; Elam, J. W.; Catillon-Mucherie, S.; Redfern, P. C.; Mehmood, F., Subnanometre platinum clusters as highly active and selective catalysts for the oxidative dehydrogenation of propane. *Nat. Mater.* **2009,** *8* (3), 213-216.
57. Smieja, J. M.; Sampson, M. D.; Grice, K. A.; Benson, E. E.; Froehlich, J. D.; Kubiak, C. P., Manganese as a substitute for rhenium in CO_2 reduction catalysts: The importance of acids. *Inorg. Chem.* **2013,** *52* (5), 2484-2491.
58. Kresse, G.; Furthmüller, J., Efficiency of ab-initio total energy calculations for metals and semiconductors using a plane-wave basis set. *Comput. Mater. Sci.* **1996,** *6* (1), 15-50.
59. Tao, J.; Perdew, J. P.; Staroverov, V. N.; Scuseria, G. E., Climbing the density functional ladder: Nonempirical meta–generalized gradient approximation designed for molecules and solids. *Phys. Rev. Lett.* **2003,** *91* (14), 146401.
60. Staroverov, V. N.; Scuseria, G. E.; Tao, J.; Perdew, J. P., Comparative assessment of a new nonempirical density functional: Molecules and hydrogen-bonded complexes. *Chem. Phys.* **2003,** *119* (23), 12129-12137.
61. Himmetoglu, B.; Floris, A.; De Gironcoli, S.; Cococcioni, M., Hubbard‐corrected DFT energy functionals: The LDA+ U description of correlated systems. *Int. J. Quantum Chem.* **2014,** *114* (1), 14-49.
62. Sun, J.; Ruzsinszky, A.; Perdew, J. P., Strongly constrained and appropriately normed semilocal density functional. *Phys. Rev. Lett.* **2015,** *115* (3), 036402.
63. Frisch, M. e.; Trucks, G.; Schlegel, H.; Scuseria, G.; Robb, M.; Cheeseman, J.; Scalmani, G.; Barone, V.; Petersson, G.; Nakatsuji, H., Gaussian 16, revision C. 01. Gaussian, Inc., Wallingford CT: 2016.
64. Weigend, F.; Ahlrichs, R., Balanced basis sets of split valence, triple zeta valence and quadruple zeta valence quality for H to Rn: Design and assessment of accuracy. *Phys. Chem. Chem. Phys.* **2005,** *7* (18), 3297-3305.
65. Becke, A. D., A new mixing of Hartree–Fock and local density-functional theories. *Chem. Phys.* **1993,** *98* (2), 1372-1377.
66. Lee, C.; Yang, W.; Parr, R. G., Development of the Colle-Salvetti correlation-energy formula into a functional of the electron density. *Phys. Rev. B: Condens. Matter* **1988,** *37* (2), 785.
67. Haoyu, S. Y.; He, X.; Li, S. L.; Truhlar, D. G., MN15: A Kohn–Sham global-hybrid exchange–correlation density functional with broad accuracy for multi-reference and single-reference systems and noncovalent interactions. *Chem. Sci.* **2016,** *7* (8), 5032-5051.
68. Ribeiro, R. F.; Marenich, A. V.; Cramer, C. J.; Truhlar, D. G., Use of solution-phase vibrational frequencies in continuum models for the free energy of solvation. *J. Phys. Chem. B* **2011,** *115* (49), 14556-14562.
69. Marenich, A. V.; Cramer, C. J.; Truhlar, D. G., Universal solvation model based on solute electron density and on a continuum model of the solvent defined by the bulk dielectric constant and atomic surface tensions. *J. Phys. Chem. B* **2009,** *113* (18), 6378-6396.